Role of phase instabilities in the early response of bulk fused silica during laser-induced breakdown

P. DeMange, R. A. Negres, R. N. Raman, J. D. Colvin, and S. G. Demos

Phys. Rev. B **84**, 054118 — Published 17 August 2011

DOI: 10.1103/PhysRevB.84.054118

The role of instabilities at the phase boundary in the early material response during laser-induced breakdown in bulk fused silica

P. DeMange, R. A. Negres, R. N. Raman, J. D. Colvin, and S. G. Demos
Lawrence Livermore National Laboratory, 7000 East Ave., Livermore, CA 94551

(Received

We report on the experimental and hydrocode modeling investigation of the early material response to localized energy deposition via nanosecond laser pulses in bulk fused silica. A time-resolved microscope system is used to acquire transient images with adequate spatial and temporal resolution to resolve the material behavior from the onset of the process. These images revealed a high-pressure shock front propagating at twice the sound speed at ambient conditions and bounding a region of modified material at delays up to one nanosecond. Hydrocode simulations matching the experimental conditions were also performed and indicated initial pressures of ~40 GPa and temperatures of ~1 eV at the absorption region. Both the simulations and the image data show a clear boundary between distinct material phases, a hot plasma and solid silica, with a suggestion that growth of perturbations at the Rayleigh-Taylor unstable interface between the two phases is the seed mechanism for the growth of cracks into the stressed solid.

Laser-induced breakdown in the bulk of transparent dielectric materials leads to exposure of the material to extreme localized conditions [1, 2]. Laser intensities in excess of 10^{11} W/cm^2 are required to achieve intrinsic breakdown in large band gap materials [3]. The absorbed energy density is high enough that the material can reach, depending on the laser parameters, localized temperatures in the 1-100 eV range and initial pressures up to 10-1000 GPa followed by the generation of a shockwave [1, 2]. This localized energy deposition is accompanied by a sequence of transient material modifications which for the case of ns excitation leads to the formation of a void and a network of cracks at delays >50 ns [4].

The transient material state during and immediately following laser energy deposition is difficult to assess with currently available analytical or experimental tools. Yet, a wide range of material science applications, from laser micro-machining and structural modification of dielectrics to laser-induced damage in high-power laser systems, depends on these fundamental behaviors. Time-resolved spectroscopy has revealed the initial steps of phase transformation of the surface of materials under fs to ps laser irradiation but our knowledge on how the material responds during and immediately after laser energy deposition in the bulk with longer (ns) pulses is very limited [5-8].

In this work, we perform direct imaging of the localized dynamics of material response in bulk fused silica following energy deposition via nanosecond pulse laser-induced breakdown. The time-resolved images reveal that the shock propagates at ≈12 km/sec for about 1 ns, followed by decay into an acoustic wave. Instabilities at the phase boundary appear to play an important role and are responsible for a faster expansion of the modified region and onset of crack formation. These crack precursors are observed to grow at a speed of ≈4.6 km/sec during the first two ns transitioning thereafter into crack propagation at ≈1.7 km/sec until termination of the process at ~20 ns delay. The experiments are complemented by hydrocode simulations to assess the pressure and temperature by a best match to the experimental results.

The experimental design to perform the time-resolved microscopic imaging experiments has been described in detail in previous work [4, 9]. A schematic of the system configuration utilized to perform this work is shown in Fig. 1. The two independent, Q-switched Nd:YAG laser systems (master and slave) were synchronized using an electronic pulse delay generator. The time-resolved microscopy system was configured for these experiments in the trans-illumination (shadowgraphy) imaging configuration. A single laser pulse (pump) at 355-nm, 3-ns time duration (at full-width-half-maximum, FWHM) from the master laser was focused within the bulk material to induce intrinsic damage on the 1-cm thick substrates. The radius ($1/e^2$) of the beam at the damage location was 5±1 μm. The energy was 535±50 μJ, corresponding to intensities up to 230-250 GW/cm^2. The calculated power is ~60 kW, well below the threshold for laser filamentation in fused silica (~5000 kW) [10]. The laser beam depth of focus

is 200-230 μm which is consistent with the observed length of the damaged region [4]. Time-resolved imaging of the transient material behavior was enabled by strobe light illumination from a 532-nm, 150-ps time duration (FWHM) slave laser. The use of ps probe pulses allowed the static spatial resolution of the system (of ≈ 1 μm) to be maintained when imaging transient phenomena up to about the speed of sound at ambient conditions in the material. The probe laser output was split into two beam paths with the second temporally delayed with respect to the first and its polarization rotated by 90 degrees. The beams were then recombined and illuminated the damage site and the surrounding volume. A composite 5X zoom and 5X objective lens system was used to collect the dual-probe signal traversing the modified material volume and subsequently filtered by a 532-nm narrowband filter to reject plasma light generated during the process. A polarizing cube beam splitter positioned after the imaging optics of the microscope separated the two image components (from each probe pulse) allowing for acquisition of two transient images per event at predetermined delays for more accurate estimation of the kinetics of the various processes involved. The images were recorded using two CCD array detectors. The time delays between pump and probe pulses were measured from their peak intensities and are quoted relative to the pump pulse (i.e., a negative delay denotes a probe pulse preceding the peak of the pump pulse).

Using a modified imaging configuration where only one linearly polarized probe was employed, we recorded the two polarization image components at a single delay time. The sum of these image components represents the conventional shadowgraphy image while the cross-polarized image allows capturing of the transient stress fields that cause rotation of the polarization orientation of the transmitted probe pulse.

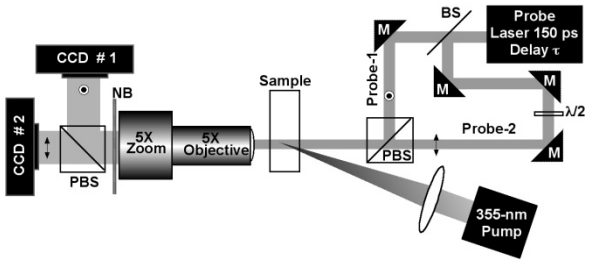

Fig. 1: Schematic of the experimental configuration used to perform this work. PBS: Polarizing Beam Splitter. M: Mirror. λ/2: Half wave plate. NB: Narrow-band filter

Figure 2 shows transient at -1.62, -0.48, 2.84, 17.9 ns delay and final (>1 second delay) images. The image at 17.9 ns delay and the final image are from the same damage site. The pump laser beam traversed left-to-right at about 30 degrees with respect to the image plane and the image focus was maintained at the tip of the emerging damage site (left hand side of images is slightly out of focus). These images depict three primary evolving features: a dark streak of modified material along the path of the high intensity beam (corresponding to what is referred to as "core" region in Ref. 4), the formation of cracks, and the propagation of a pressure wave. The image at -1.62 ns delay shows a dark region already forming and bounded by a pressure wave propagating laterally. A small perturbation along the boundary of the modified material can also be observed. The image captured at -0.48 ns delay shows the growth of the perturbations and a departure of the pressure wave from the dark region. As it will be discussed later in more detail, these perturbations act as crack precursors, as their position corresponds to where cracks later develop. At 2.84 ns delay, the image shows no further growth of the dark region but a development of projections from the perturbations observed at earlier delays. The pressure wave is propagating as a spherical wave at the damage site tip. The image at 17.9 ns delay shows well-developed cracks bounding the dark region at the previously observed projections. The final image shows the cracks at full size, only slightly larger than at 17.9 ns delay.

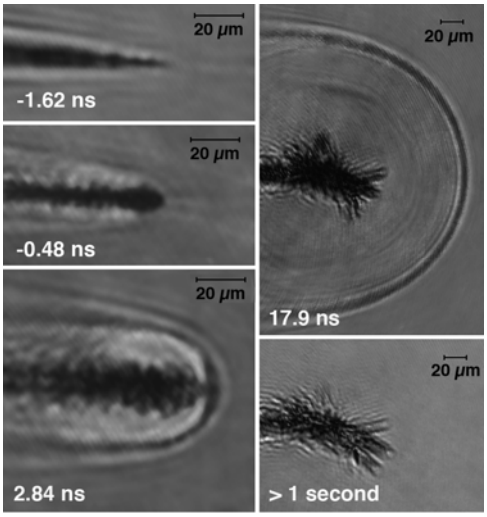

Fig. 2: Transient images of the damage region induced by the 355-nm, 3-ns pulse in the bulk of fused silica acquired at different delays.

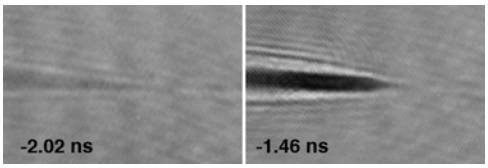

Fig. 3: Transient images of the same event acquired at two different delays during the buildup of the electronic excitation of the material. The image dimensions are 150 μm × 100 μm.

Figure 3 shows a typical example of our observations at early delays, prior to the launch of a shockwave. These images were acquired during the same event at delays of -2.02 ns and -1.46 ns. The first image (left) was provided by probe 1 and demonstrates the presence of a transmission loss near the focal point of the pump beam manifested as a slightly darker feature in the shadowgraphy image. The second image (right) was provided by probe 2 (arriving 560 ps later) and clearly indicates that the transmission loss has increased with time. These two images acquired at early delay times are representative of the initial phase of material modification within the pump focal region, namely onset and increase in probe transmission loss to over 95% within about 700 ps. We postulate that this early phase is associated with the buildup of the electronic excitation of the material as noted in Ref. 11 associated with increase in the localized temperature and absorptivity.

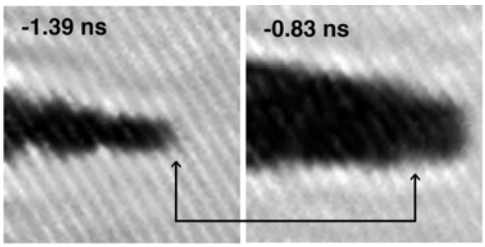

Fig. 4: Transient images of the same event acquired at two different delays during the onset of the formation of the damage site. The image dimensions are 30 μm × 30 μm.

The next step in the early material modification process is associated with the observation of a dark region at the tip of the conical absorbing region (shown in Fig. 4 and assigned to the build up of the electronic excitation) that is characterized by a slightly irregular interface with the surrounding volume. This region immediately starts to expand in all dimensions. A typical example of this process is demonstrated by the image acquired at -1.39 ns (left) shown in Fig. 4. The image of the same site acquired at -0.83 ns delay (Fig. 4, right side) captures the expansion of this region which is clearly faster along the beam propagation (axial) direction. This is a common observation in our experiments at the beginning of this process when the core region of the damage site is established. Within a few hundreds of ps, the initial core region of the damage site reaches its final axial dimensions (but subsequently is observed to radialy expand as discussed next). It was difficult to better resolve this process in our experiments as its temporal evolution was comparable to the probe pulse duration. The arrows in Fig. 4 correspond to the same axial position in both images and are used to demonstrate the axial expansion of the core region. The radial (transverse) expansion of the site is also evident and is manifested by the widening of the dark volume in the second transient image of the site compared to the first one. We were not able to capture the axial expansion in the backward direction as it is hidden by the transmission loss associated with the buildup of the electronic excitation (shown in Fig. 3). The stripes observed in the images shown in Fig. 4 are an artifact arising from the image normalization process used.

Figure 5 shows shadowgraphy images of the same site acquired at two different delay times during the early phase of the shockwave expansion. The time separation between these images is 560 ps and the spatial expansion at the tip of the emerging site is on the order of twice the speed of sound at ambient conditions in this material (12 km/sec). At this early stage it is impossible to distinguish between the expanding shock front and the expanding core (central) region of the modified material which becomes visible at later delays. However, the outer surface of this region corresponds to the location of the shock front. It must be noted that the expansion of the site at the time is symmetric, in contrast with the observation at earlier times (see Fig. 4). Consequently, the radial expansion of the shock wave at this early time can be quantified by fitting a circle at the right tip of the expanding region and using its radius as the assumed distance traveled by the shockwave.

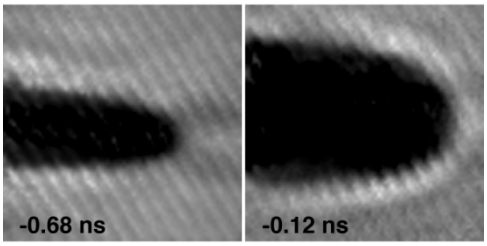

Fig. 5: Transient images of the same event acquired at two different delays illustrating the onset of shockwave expansion. The image dimensions are 30 μm × 30 μm.

Figure 6 shows un-polarized (left) and cross-polarized (right) images of the same site at the same delay (4.38 ns). The unpolarized image is the conventional shadowgraphy image. The corresponding

cross-polarized image is presented in logarithmic intensity scale to enhance the visibility of all features. This image arises from the presence of stress that causes the rotation of polarization of the illumination probe light. The similarity in the spatial features in the dark core region of modified material is apparent. These features are somewhat better visualized in the cross-polarized image because the volume outside this region is under stress and provides high image contrast. This contrast also allows for a better visualization of the interface between the core (hot) region and the surrounding cold material under stress. Both images are able to capture the shock (pressure) front but its appearance is different in these images. In the unpolarized image, light scattering in the pressure wave due to material density variations generates a bright-then-dark expanding front. In the cross-polarized image, the stress from the pressure wave causes depolarization of the illumination light and can be seen in the image as a bright expanding front. The exact correlation of these features is provided in Fig. 6 with the use of two arrows that correspond to the same spatial location in the two images.

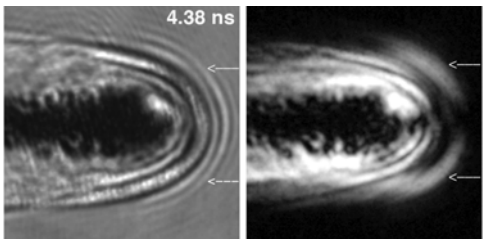

Fig. 6: Unpolarized (left) and cross-polarized (right) transient images of the same site at 4.38 ns delay. The intensity in the cross-polarized image is in logarithmic scale. The arrows indicate the spatial correlation of the images at the pressure wave front. The image dimensions are 100 μm × 100 μm.

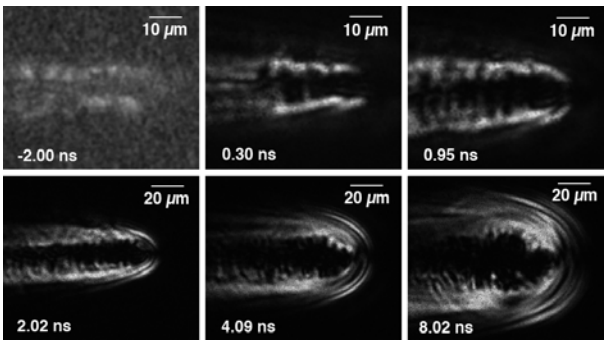

Fig. 7: Cross-polarized images of different but similar laser-induced breakdown events at various delays.

Figure 7 shows cross-polarized transient images of different but similar breakdown events at various delays as indicated in the images. All images are in linear intensity scale and their contrast has been individually adjusted to enhance visibility of the dominant features. The first image captured at -2.00 ns delay indicates that the stress is building up from the early times corresponding to the onset of the electronic excitation (as shown in Fig. 3). This indicates that the buildup of the electronic excitation is associated with the development of stress in the surrounding region, which may be an indication that the localized temperature in the central region is increasing. In addition, the degree of depolarization seems to vary between neighboring locations (manifested as variability in the intensity in the cross-polarized image) which may be an indication that the localized temperature is different within the central region giving rise to a variable amount of stress in the corresponding surrounding region. This variability may originate from an early non-uniform absorption of the laser pulse energy within the focal region or non-uniformities in the incident beam intensity.

Our results indicate that during the buildup of the electronic excitation (and before the launch of the shockwave) the increase of the transmission loss, exemplified in Fig. 3, is accompanied by an increase in the strength of the depolarization signal observed in the cross-polarized images. This increase remains localized with no spatial expansion within the resolution of our imaging system.

In the next two images shown in Fig. 7 captured at 0.30 ns and 0.95 ns delays, the development of instabilities at the interface between the expanding region of modified (hot) material and the surrounding (cold) material is clearly visible. The stress at the tips of these instabilities causes a strong depolarization of the light. In addition, it appears as if secondary pressure fronts originate at each of these instabilities (projections). The image at 2.02 ns delay shows the projections formed within the central region of the modified material behind the shockwave. The latter appears as a bright band but there are several succeeding waves which may have formed from the secondary pressure fronts generated at the tips of the projections as they rapidly expand during the initial few ns of the process. The last two images in Fig. 7 were acquired at 4.09 ns and 8.02 ns delays and show further growth of the projections but their width is narrowed as they develop into cracks. The initial shockwave accompanied by secondary waves continues to propagate but no additional stress waves are being generated at later delay times. Furthermore, the core region of modified material has reached its maximum size.

Figure 8 shows the as-measured lateral distance (relative to the pump beam path) of the pressure wave, crack tip, and outer edge of the dark absorbing region as

a function of delay, along with the temporal trace of the pump pulse. The position of the pressure wave was obtained from its radius of curvature of the spherically propagating pressure wave from the tip (right side) of the damage site, as discussed earlier. The red data points in Fig. 8 indicate a "pre-damage effect" in which a faint darker region was observed without a pressure wave, as discussed earlier in relation to Fig. 3. In the inset (zoom-in at early delays), two linear fits (with different slopes) to the shock and crack radius data are shown over different time delay intervals and indicate distinct expansion speeds. For the pressure wave, a fit between -1.4 and -0.6 ns delay has a slope of ≈11.9 μm/ns and the fit beyond 1 ns delay has a slope of 5.9 μm/ns (the speed of sound at ambient conditions in fused silica). The crack growth is separated into two phases. The early phase is associated with the growth of the crack precursors (assigned to instabilities at the phase boundary) during the first few nanoseconds with an average speed of ≈4.6 μm/ns. This is followed by a slower growth of the cracks, at ≈1.7 μm/ns, up until ~25 ns delay. The cracks reach an average radius of 48 μm. The latter speed of the crack growth is about 1/3 of the sound speed and reasonable for stress intensities in excess of the fracture toughness of the material [12].

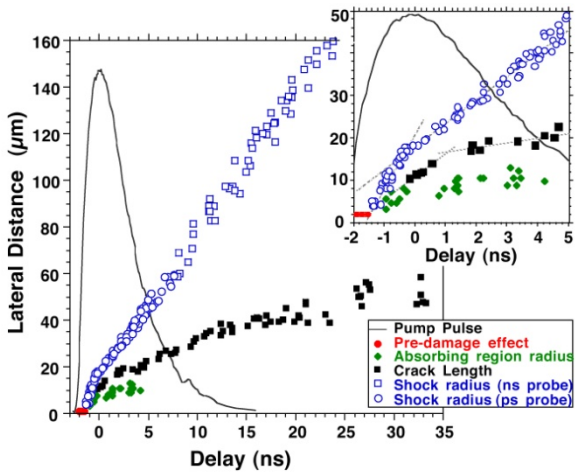

Fig. 8: Lateral distance of the pressure wave, crack tip, and outer edge of core region of modified material as a function of delay time, along with the temporal profile of the pump pulse.

Simulations in 2D axisymmetric geometry were performed using ALE3D finite element hydrocode and applying the experimental conditions. The material parameters in the simulations were varied to investigate how to reproduce the rapid radial expansion during the first nanosecond measured from the transient images. The code applied solutions to the hydrodynamic and heat equations in the Lagrange mesh motion formulation and used an explicit time integration method. A ray tracing algorithm for the laser beam was used in the code with the beam convergence and Gaussian spot size from the experiment implemented as a table of values, each at a corresponding depth within bulk fused silica. The laser absorption, thermal conductivity, and heat capacity were implemented as a table of values at corresponding temperatures. For the base case simulation, these parameters were fit to an exponential, according to experimental measurements [13-15], and extrapolated to eV temperatures. A solid phase, tabular-form equation of state was used with a Grueneisen gamma model at low temperature and Thomas-Fermi model at high temperature [16]. For all material data, the code applied a cubic interpolation fit.

In the simulations, the laser absorption coefficient (at 300 K) was tuned such that the onset of absorption during the laser pulse coincides with the time of the earliest measurement of the shock radius from the experiment. As seen from the inset of Fig. 8, this latter parameter was -1.4 ns, or 1.4 ns before the peak intensity of the laser pulse. The simulations showed that the absorption leads to temperatures of thousands of degrees and GPa pressures within 0.2 ns, which is therefore the time window of uncertainty in the alignment with experiment.

Figure 9 shows a pseudocolor scale pressure and temperature image from the base case hydrocode simulation with the extrapolated exponential fits to the material parameters (top) and a transient image of a damage site (bottom), both at 0.32 ns delay with respect to the pump peak intensity. The image from the simulation shows that the pressure front extends laterally to 4.8 μm, which is 5.0 μm shorter than measured in the recorded image from the experiment (at 9.8 μm). This discrepancy highlights a much lower lateral speed of the pressure wave in the simulation, which is calculated to be close to the sound speed at ambient conditions as opposed to about twice the speed of sound found in the experiment. The simulation predicts that the peak pressure of the lateral shock wave in the image is 39 GPa. The temperature portion, in the upper half of the image, shows a large region at temperature greater than 10^4 K (maximum brightness on color scale). This region is well above the melting temperature with the maximum temperature estimated to be 1.3 eV (1.5×10^4 K). Outside of this region the material remains in the solid phase (well below melt). The high-temperature region extends laterally with a radius of 3.3 μm and is consistent with the size of the dark core region in the

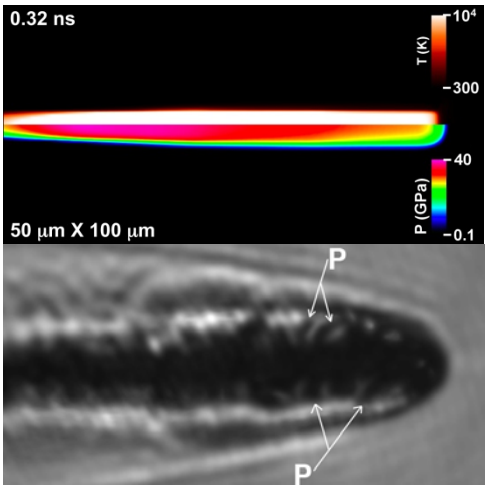

Fig. 9: Images of the pressure and temperature from simulation (above) and a damage site from experiment (below), both at 0.32 ns delay. Early crack projections are indicated in the data image.

experimental image. The image from the experiment shows that the boundary of the core region (uniformly dark) that divides the two material phases is not smooth as predicted in the simulation but has multiple projections pointing away from the center and extending as much as twice the radius of the core region. These projections reach as far out as the shock front (as shown in Fig. 9) and are even seen at the shock front at earlier delays such as shown in the image at -1.62 ns in Fig. 2. The results indicate that some of these projections evolve to cracks at later delays. The simulation clearly is not able to capture the physics of these projections which evidently has a significant effect on the size and subsequent expansion of the absorption region.

Experimental error is primarily in the pump intensity due to spot size and laser pulse energy, which may be reflected in the input values used in the simulation, in addition to other sources of error due to shortcomings in the code models and the equation of state and other data. However, simulations performed varying the dependence on temperature of the absorption coefficient and other material parameters mostly showed no significant change in pressure or temperature, or pressure wave speed from the base case simulation. The only differing case used a rapid exponential increase in absorption coefficient with temperature, which did not change the lateral expansion of the absorption region but gave a more rapid longitudinal expansion than observed in the experimental images. Nonetheless, this resulted in a negligible change to the maximum temperature and pressure. Similar variations to either the heat capacity or thermal conductivity of the material were unable to change the results significantly. Radiation transport was not included in the simulation but other experiments suggest that this should not be a notable effect at the temperatures involved [1]. An absorption coefficient (κ) of 4.4×10^{-2} cm^{-1} at 300 K was the best fit value for synchronizing the simulations to the experiment. This value is consistent with experimental measurements in Refs. 17 and 18 for silica with the same laser parameters.

The experimental results indicate material evolution in multiple stages during the first 50 ns following laser-induced breakdown leading to irreversible material modification (damage). The first nanosecond is marked by a pressure absorption front wave propagating from the absorption region at twice the sound speed accompanied by the formation and expansion of projections in the core region. At delay greater than 1 ns from the onset of the process, the pressure wave propagates at the acoustic speed and a linear growth of cracks take place up to ~20 ns delay. After ~2 ns, the damaged region is completely defined minus the remaining crack growth, reaching the size and form observed post-mortem.

The projections, or crack precursors, grow from the outer boundary of the absorbing region, which is the dark region in the recorded image from the experiment in Fig. 9. This void boundary is also, as discussed above, a phase boundary between the hot lower-density plasma on the inside and the cooler solid or liquid silica on the outside. The projections are indicative of the development and growth of instabilities at this phase boundary. In contrast to these experimental observations, the image from the simulation in Fig. 9 shows no hints of the formation of instabilities. The temperature pseudo-color scale in the top half of the image shows a smooth profile over the core region. Similarly, in the pressure pseudo-color bottom half of the image, the pressure wave is without variation and smooth along the front. The pressure wave speed from the simulation is calculated to be on the order of the sound speed at ambient conditions, half of that measured in experiment during its initial phase of expansion. This may suggest a correlation between the growth of the instabilities and subsequent formation of the projections.

Simulations performed with a better focus toward capturing the growth of the instabilities at the phase boundary were unsuccessful. The instabilities were seeded by applying a non-uniform absorption coefficient at 5 μm spatial intervals, the approximate width of the projections measured from the experimental images. A strength model for fused silica was used to improve the solid state material response and fine spatial zoning of 10 zones/micron was applied to better resolve the development of the instabilities. The simulations showed that the varying amounts of non-uniformity of the absorption coefficient gave as large as ~10 GPa pressure

differences between regions without any indication of instability growth. This demonstrates that there are several key factors contributing to the development of the instability that are not being captured either accurately or at all in the hydrocode. Instabilities can be seeded by factors such as non-uniform absorption coefficient, material variations or non-uniform beam intensity. Moreover, the absence of an accurate strength model for fused silica, an available EOS that accounts for material phase transitions, and models for work hardening and crack formation may inhibit the development of instabilities using the hydrocode.

Nonetheless, the simulation in Fig. 9 shows a large temperature difference between the core region and the surrounding matrix clearly indicative of the phase boundary where the instabilities in the experiment develop. The interface of the phase boundary in the simulation is being pushed outward by material at ~eV temperature equivalent to a hot plasma during the initial rise of the laser pulse to peak power. This indicates that this interface is classically Rayleigh-Taylor (RT) unstable. We can estimate the linear-phase growth rate of strength-stabilized RT, assuming negligible equivalent lattice viscosity, from the formulation given in Ref. 19 as $\gamma=[kAa-k^2G/\rho_s]^{1/2}$. The wavelength of the perturbations, $\lambda=2\pi/k$, is the spacing of the projections, ~5 μm; the simulation provides an estimate of the densities on either side of the interface (ρ_p~1.5 g/cm^3 in the plasma, ρ_s~2.9 g/cm^3 in the liquid/solid) from which we estimate the Atwood number as A~0.3; the acceleration of the interface is estimated from the data shown in Fig. 2 as a~10 μm/ns^2. If the hot plasma is pushing on liquid silica, the shear modulus of the silica is G~0, from which we can estimate a maximum growth rate of the perturbations of γ~2 ns^{-1}. As seen in the image data, the perturbation growth is already non-linear by the time the projections first become visible, at ~-0.5 ns, so to be consistent with this estimated growth rate, the perturbations would have to have had initial amplitude of at least ~0.5 μm. This is not inconsistent with the probable spatial scale of the non-uniformities in the energy deposition. The RT growth stops as the interface stops accelerating. By this time, however, the RT instability has left a non-uniform residual stress state in the silica, and the cracks are seen to grow as extensions of these RT-seeded projections.

The experiment in this work has shown that there are distinct phases in the material modification process associated with laser-induced breakdown in the bulk of fused silica. These involve a) the buildup of the electronic excitation, b) the establishment of the core region of the damage site, c) the launch of the shockwave accompanied by an expansion of the central region and onset of instabilities at the phase boundary, d) growth of the instabilities at the phase boundary which give rise to secondary pressure waves and, e) initiation and propagation of cracks as an extension of the instabilities at the phase boundary. The mechanical nature of damage originates at early times at a small region under extreme pressure and temperature, and on a time scale of less than 1 ns. The simulations, although they are not able to capture the mechanical nature or the instability growth, have been able to further support measurements in providing comparable pressures and temperatures as well as spatial and temporal scales to those measured experimentally. The growth of Rayleigh-Taylor instability is consistent with our results and may be the mechanism for the initiation of cracks.

This work was performed under the auspices of the U.S. Department of Energy by Lawrence Livermore National Laboratory under Contract DE-AC52-07NA27344.

[1] C. W. Carr, H. B. Radousky, A. Rubenchik, M. D. Feit, and S. Demos, Phys. Rev. Lett. **92**, 087401 (2004).
[2] S. Juodkazis, K. Nishimura, S. Tanaka, H. Misawa, E. G. Gamaly, B. Luther-Davies, L. Hallo, P. Nicolai, and V. T. Tikhonchuk, Phys. Rev. Lett. **96**, 166101 (2006).
[3] B. C. Stuart, M. D. Feit, A. M. Rubenchik, B. W. Shore, and M. D. Perry, Phys. Rev. Lett. **74**, 2248 (1995).
[4] R. A. Negres, M. D. Feit, and S.G. Demos, Opt. Exp. **18**, 10642 (2010).
[5] H. Ihee, et al., Science **291**, 458 (2001).
[6] A. M. Lindenberg, et al. Science **308**, 392 (2005).
[7] D. Perez and L. J. Lewis, Phys. Rev. Lett. **89**, 255504 (2002).
[8] K. Sokolowski-Tinten, J. Bialkowski, A. Cavalleri, and D. von der Linde, A. Oparin, J. Meyer-ter-Vehn, and S. I. Anisimov, Phys. Rev. Lett. **81**, 224 (1998).
[9] R.N. Raman, R.A. Negres, and S.G. Demos, Opt Eng 50, 013602 (2011).
[10] R. W. Boyd, *Nonlinear Optics*, Academic Press (2003).
[11] X. Mao, S. S. Mao, and R. E. Russo, Appl. Phys. Lett. **82**, 697 (2003).
[12] B. Lawn, Fracture of Brittle Solids, 2nd Ed., Cambridge University, Cambridge, 1993.
[13] E. Beder, C. Bass, and W. Shackleford, J. Am. Ceram. Soc. **10,** 2263–2268 (1971).
[14] S. T. Yang, M. J. Matthews, S. Elhadj, V. G. Draggoo, and S. E. Bisson, J. Appl. Phys. **106**, 103106 (2009).
[15] H. T. Smyth, H. S. Skogen, and W. B. Harsell, J. Am. Ceram. Soc. **36**, 327 (1953).
[16] D. A. Young and E. M. Corey, J. Appl. Phys. **78**, 3748 (1995).
[17] M. Khashan and A. Nassif, Opt. Commun. **188,** 129–139 (2001).

[18] R. Kitamura, L. Pilon, and M. Jonasz, Appl. Opt. **46**, 8118 (2007).
[19] J. D. Colvin, M. Legrand, B. A. Remington, G. Schurtz, and S. V. Weber, J. Appl. Phys. 93, 5287 (2003).